EXPANSION OF BUNDLES OF LIGHT RAYS IN THE LEMAÎTRE–TOLMAN MODELS

Andrzej Krasiński

N. Copernicus Astronomical Centre, Polish Academy of Sciences,
Bartycka 18, 00-716 Warszawa, Poland
(e-mail: akr@camk.edu.pl)

(*Received March 17, 2021 — Revised August 5, 2021*)

The locus of $\theta \stackrel{\text{def}}{=} k^{\mu}{}_{;\mu} = 0$ for bundles of light rays emitted at noncentral points is investigated for Lemaître–Tolman (L–T) models. The three loci that coincide for a central emission point: (1) maxima of R along the rays, (2) $\theta = 0$, (3) $R = 2M$ are all different for a noncentral emitter. If an extremum of R along a nonradial ray exists, then it must lie in the region $R > 2M$. In $2M < R \leq 3M$ it can only be a maximum; in $R > 3M$ both minima and maxima can exist. The intersection of (1) with the equatorial hypersurface (EHS) $\vartheta = \pi/2$ is numerically determined for an exemplary toy model (ETM), for two typical emitter locations. The equation of (2) is derived for a general L–T model, and its intersection with the EHS in the ETM is numerically determined for the same two emitter locations. Typically, θ has no zeros or two zeros along a ray, and becomes $+\infty$ at the Big Crunch (BC). The only rays on which $\theta \to -\infty$ at the BC are the radial ones. Along rays on the boundaries between the no-zeros and the two-zeros regions θ has one zero, but still tends to $+\infty$ at the BC. When the emitter is sufficiently close to the center, θ has 4 or 6 zeros along some rays (resp. 3 or 5 on the boundary rays). For noncentral emitters in a collapsing L–T model, $R = 2M$ is still the ultimate barrier behind which events become invisible from outside; loci (1) and (2) are not such barriers.

Keywords: general relativity, cosmological models, light propagation, horizons.

1. Motivation and background

We are interested in the outer boundary of a set whose every point lies in a trapped surface (the latter is a 2-surface whose family of outgoing orthogonal light rays has nonpositive expansion scalar). With a slight abuse of the original definition [1] we will refer to this as the apparent horizon (AH).

In the Lemaître [2]–Tolman [3] (L–T) models the AH has been so far considered only for bundles of light rays emitted at the world line of the central observer [4, 5]. In this case, the AH can be defined in two ways:

(1) As the locus where the surface areas of the light fronts of the bundles achieve maxima. At the same locus the areal radius R of the light front becomes maximum.

(2) As the locus where the expansion scalars $\theta \stackrel{\text{def}}{=} k^{\mu}{}_{;\mu}$ of such bundles become zero (k^{μ} is the vector field tangent to the rays).

Both these definitions determine the same hypersurface $R = 2M$.

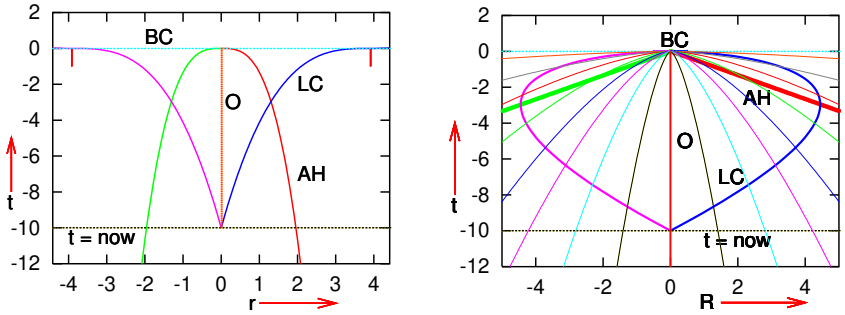

Fig. 1. Left panel: Profiles of the future apparent horizon AH of a comoving observer O and of the future light cone LC of O's present instant in the collapsing Friedmann model (1.1). **Right panel:** The same situation in the (t, R) variables where $R = rS(t)$. At the AH R becomes maximum along the rays. See the text for more explanation.

This created the impression that the AH so defined is common to all light emitters. However, in Friedmann models [6], which are the spatially homogeneous limits of L–T models, each observer is central because of the homogeneity and each one has a differently located AH. The exemplary model used for Fig. 1 has the metric

$$ds^2 = dt^2 - S^2(t)\left[dr^2 + r^2\left(d\vartheta^2 + \sin^2\vartheta d\varphi^2\right)\right] \tag{1.1}$$

with $S(t) \propto (t_{\rm BC} - t)^{2/3}$, $t_{\rm BC}$ is the Big Crunch time. In the left panel the (t, r) coordinates are comoving. The future light cone LC of the present instant of observer O hits the BC tangentially at r values marked by the vertical strokes. In the right panel the coordinates are t and the areal radius $R = rS(t)$, the BC is a single point and the AH profile is the pair of straight lines. The curves converging at the BC are world lines of particles of the cosmic medium — in the left panel they would be vertical straight lines. Such structures exist around every comoving observer world line in any collapsing Friedmann model.

So, it was puzzling where the AH would be for a noncentral observer in an L–T model. The present paper aims at answering this question. The loci of extrema of R and of $\theta = 0$ in L–T models are here investigated for bundles of rays that originate at noncentral events. Then, sets (1), (2) and (3) the locus of $R = 2M$ are all different[1]. This is illustrated using the explicit L–T toy-model (ETM), first introduced in [4].

In Section 2, basic information about the L–T models is given. In Section 3, the equations of null geodesics in these models are written out and prepared to numerical integration. In Section 4, the equation defining a local extremum of the areal radius R along a light ray is discussed for a general L–T model. It is shown that on nonradial rays an extremum can exist only in the $R > 2M$ region. If it

[1] The loci of $\theta = 0$ and of extremum of D_a — the area distance from the origin O of the ray bundle — do coincide [7]. But if O is not at the center of symmetry, then $D_a \neq R$ and their extrema split.

occurs in $R < 3M$, then it is necessarily a maximum. In $R > 3M$ both minima and maxima are possible (but need not exist).

In Section 5 the loci of extrema of R are discussed for the ETM. They are numerically calculated for rays running in the equatorial hypersurface $\vartheta = \pi/2$ (EHS), in the recollapse phase of the model. On some nonradial rays R monotonically decreases to 0 achieved at the BC. On some other rays, R has only maxima, on still other ones it has both minima and maxima. The latter can happen when the ray leaves the light source toward decreasing R (which is impossible when the source is at the center where $R = 0$).

In Section 6, the equation of the locus of $\theta = 0$ for a bundle of light rays in a general L–T model is derived. Except on outward radial rays, it does not coincide with the locus of an extremum of R. A method to numerically calculate θ along a nonradial ray is given; an auxiliary nearby ray is needed for that.

In Section 7, the $\theta = 0$ equation is numerically solved for rays running in the EHS of the ETM used in Section 5. Typically, θ has no zero or two zeros along a ray, and becomes $+\infty$ at the Big Crunch (BC), so the ray bundle is infinitely *diverging* at the BC. The only rays on which $\theta \to -\infty$ at the BC are the radial ones. Along rays on the boundaries between the no-zeros and the two-zeros regions θ has one zero, but still tends to $+\infty$ at the BC. When the emitter is sufficiently close to the center, θ has 4 or 6 zeros along rays passing near the center (resp. 3 or 5 on the boundary rays). The loci of θ-zeros and temporal orderings of loci (1)–(3) along various rays are displayed for exemplary emission points of the ray bundles. A locus of $\theta = 0$ may lie earlier or later than $R = 2M$ and than the maximum of R, depending on the initial direction of the ray.

In Section 8 the results of the paper are summarised and discussed. One of the conclusions is that the hypersurface $R = 2M$ still is an AH for noncentral emitters. Namely, if $\theta = 0$ occurs at a point p_1 in the region $R > 2M$, then the radial ray sent outwards from p_1 will proceed some distance toward larger R — which means that p_1 is not yet locally trapped. On the other hand, if $\theta = 0$ occurs at p_2 in the region $R < 2M$, then events along this ray became invisible from outside before the ray reached p_2. Thus, in a collapsing L–T model, $R = 2M$ is the ultimate barrier from behind which no light rays can get to the outside world; the loci of maximum R and of $\theta = 0$ are not such barriers.

2. Basic properties of the Lemaître–Tolman models

The L–T models [2, 3, 5] are spherically symmetric nonstatic solutions of the Einstein equations with a dust source. Their metric is

$$ds^2 = dt^2 - \frac{R_{,r}{}^2}{1 + 2E(r)} dr^2 - R^2(t,r)(d\vartheta^2 + \sin^2\vartheta d\varphi^2), \tag{2.1}$$

where $R(t,r)$ is determined by the equation

$$R_{,t}{}^2 = 2E(r) + 2M(r)/R + \Lambda R^2/3; \tag{2.2}$$

$E(r) \geq -1/2$ and $M(r)$ are arbitrary functions, $R_{,r} \stackrel{\text{def}}{=} \partial R/\partial r$, $R_{,t} \stackrel{\text{def}}{=} \partial R/\partial t$, and Λ is the cosmological constant. The mass-density is

$$\kappa\rho = \frac{2M_{,r}}{R^2 R_{,r}}, \qquad \text{where } \kappa \stackrel{\text{def}}{=} \frac{8\pi G}{c^4}. \tag{2.3}$$

In the following we assume $\Lambda = 0$. Then (2.2) can be solved in terms of elementary functions [5]. We will use only an $E < 0$ solution, in which

$$R(t,r) = \frac{M}{(-2E)}(1 - \cos\eta), \tag{2.4}$$

$$\eta - \sin\eta = \frac{(-2E)^{3/2}}{M}\left[t - t_B(r)\right], \tag{2.5}$$

where η is a parameter and the arbitrary function $t_B(r)$ determines the local Big Bang (BB) instant at $t = t_B(r)$. This model is initially expanding and later collapses to the final singularity (BC) at $t = t_C(r)$. Writing (2.5) at $\eta = 2\pi$ where $t = t_C$ we obtain

$$2\pi = \frac{(-2E)^{3/2}}{M}\left[t_C(r) - t_B(r)\right], \tag{2.6}$$

so of the four functions M, E, t_B and t_C only three are independent.

All the formulae above are covariant under the transformations $\tilde{r} = g(r)$, so we can give one of the three functions $E(r)$, $M(r)$ and ($t_B(r)$ or $t_C(r)$) a convenient shape. In our exemplary toy model introduced in Section 4, it will be convenient to take $\tilde{r} = M(r)$.[2]

The Friedmann models [6] are contained in the L–T class as the limit:

$$t_B = \text{constant}, \qquad |E|^{3/2}/M = \text{constant}, \tag{2.7}$$

and with $M = \text{constant} \times r^3$ their most popular coordinate representation results.

Shell crossings (SCs), are loci at which neighbouring constant-r shells collide. At a SC, $R_{,r} = 0 \neq 1 + 2E$; they are curvature singularities. The conditions on M, E and t_B that ensure the absence of SCs were given in [8], and will be used below.

3. Light rays in an L–T model

The tangent vectors $k^\alpha = dx^\alpha/d\lambda$ to geodesics of the metric (2.1) obey

$$\frac{dk^t}{d\lambda} + \frac{R_{,r}\,R_{,tr}}{1+2E}\;(k^r)^2 + RR_{,t}\;\left[(k^\vartheta)^2 + \sin^2\vartheta\;\;(k^\varphi)^2\right] = 0, \tag{3.1}$$

$$\frac{dk^r}{d\lambda} + 2\frac{R_{,tr}}{R_{,r}}\;k^t k^r + \left(\frac{R_{,rr}}{R_{,r}} - \frac{E_{,r}}{1+2E}\right)\;(k^r)^2 - \frac{(1+2E)R}{R_{,r}}\;\left[(k^\vartheta)^2 + \sin^2\vartheta\;\;(k^\varphi)^2\right] = 0, \tag{3.2}$$

[2]Such a choice of the radial coordinate is allowed in those ranges of r where the function $M(r)$ is monotonic. In the model of Section 4 this problem does not arise as the range of M is $[0, \infty)$ and no other radial coordinate appears.

$$\frac{dk^{\vartheta}}{d\lambda} + 2\frac{R_{,t}}{R}\ k^t k^{\vartheta} + 2\frac{R_{,r}}{R}\ k^r k^{\vartheta} - \cos\vartheta \sin\vartheta\, (k^{\varphi})^2 = 0, \tag{3.3}$$

$$\frac{dk^{\varphi}}{d\lambda} + 2\frac{R_{,t}}{R}\ k^t k^{\varphi} + 2\frac{R_{,r}}{R}\ k^r k^{\varphi} + 2\frac{\cos\vartheta}{\sin\vartheta}\ k^{\vartheta} k^{\varphi} = 0, \tag{3.4}$$

where λ is the affine parameter. The geodesics are null when

$$\left(k^t\right)^2 - \frac{R_{,r}{}^2 (k^r)^2}{1+2E} - R^2\left[(k^{\vartheta})^2 + \sin^2\vartheta\, (k^{\varphi})^2\right] = 0. \tag{3.5}$$

Since $R_{,t}\, k^t + R_{,r}\, k^r = dR/d\lambda$, the general solution of (3.4) is

$$R^2 \sin^2\vartheta k^{\varphi} = J_0, \tag{3.6}$$

where J_0 is constant along the geodesic. The case $J_0 = 0$ corresponds to two situations:

(a) $\vartheta = 0, \pi$; then the ray stays on the axis of symmetry, with undetermined φ.

(b) $k^{\varphi} = 0$ with ϑ (as yet) unspecified; then the ray stays in a constant-φ hypersurface.

Using (3.6), the general solution of (3.3) is

$$R^4 (k^{\vartheta})^2 \sin^2\vartheta + J_0{}^2 = C^2 \sin^2\vartheta, \tag{3.7}$$

where C is another constant along the geodesic. When $C = 0$, the geodesic is radial. Then $J_0 = 0$ and either (a) $\vartheta = 0, \pi$, or (b) ϑ is constant along the ray and φ is constant by (3.6). When $C = \pm J_0 \neq 0$, the geodesic remains in the equatorial hypersurface $\vartheta = \pi/2$ (which is not flat even when $E = 0$). For later reference let us note the following:

The coordinates (ϑ, φ) can be adapted to any single geodesic so that it stays in the hypersurface $\vartheta' = \pi/2$ in the new coordinates (ϑ', φ'). (3.8)

This is a consequence of spherical symmetry of the spacetime [5]. Eq. (3.7) implies

$$C^2 \sin^2\vartheta \geq J_0{}^2. \tag{3.9}$$

For rays with $J_0 \neq 0$, Eq. (3.6) implies in addition

$$k^{\varphi} \equiv \frac{d\varphi}{d\lambda} \to \infty \qquad \text{when} \qquad R \to 0. \tag{3.10}$$

Thus, if $|dr/d\lambda| < \infty$ at the intersection with the BB or BC, then $d\varphi/dr \underset{t\to t_B}{\longrightarrow} \infty$, i.e. these rays meet the singularity being tangent to a surface of constant r.

Eqs. (3.3) and (3.4) are now solved. From (3.6) and (3.7) we get

$$(k^{\vartheta})^2 + \sin^2\vartheta\, (k^{\varphi})^2 = C^2/R^4, \tag{3.11}$$

and then (3.5) becomes

$$\left(k^t\right)^2 = \frac{R_{,r}{}^2 (k^r)^2}{1+2E} + \frac{C^2}{R^2}. \tag{3.12}$$

Eqs. (3.1)–(3.2), using (3.6)–(3.12), simplify to

$$dt/d\lambda = k^t, \tag{3.13}$$

$$\frac{dk^t}{d\lambda} = \left[(C/R)^2 - \left(k^t\right)^2\right] \frac{R_{,tr}}{R_{,r}} - \frac{C^2 R_{,t}}{R^3}, \tag{3.14}$$

$$dr/d\lambda = k^r, \tag{3.15}$$

$$\frac{dk^r}{d\lambda} = -2\frac{R_{,tr}}{R_{,r}}\ k^t k^r - \left(\frac{R_{,rr}}{R_{,r}} - \frac{E_{,r}}{1+2E}\right)\ (k^r)^2 + \frac{C^2(1+2E)}{R^3 R_{,r}}. \tag{3.16}$$

The initial data for (3.13)–(3.16) are t, r, k^t and k^r at the initial point of the ray $(t, r, \vartheta, \varphi) = (t_o, r_o, \vartheta_o, \varphi_o)$. In numerical calculations, (3.12) will be used at every step to correct the value of k^t found by integrating (3.13)–(3.16).

One more initial condition is achieved by rescaling λ,

$$k^t(t_o) = \pm 1 \tag{3.17}$$

(+ for future-directed, − for past-directed rays). With (3.17) we have from (3.12),

$$C^2 \le R^2(t_o, r_o) \overset{\text{def}}{=} {R_o}^2; \tag{3.18}$$

the equality occurs when $k^r(r_o) = 0$.

The following formulae [5] are useful in numerical calculations:

$$R_{,r} = \left(\frac{M_{,r}}{M} - \frac{E_{,r}}{E}\right) R + \left[\left(\frac{3}{2}\frac{E_{,r}}{E} - \frac{M_{,r}}{M}\right)(t - t_B) - t_{B,r}\right] R_{,t}\,, \tag{3.19}$$

$$R_{,tr} = \frac{E_{,r}}{2E}\ R_{,t} - \frac{M}{R^2}\ \left[\left(\frac{3}{2}\frac{E_{,r}}{E} - \frac{M_{,r}}{M}\right)(t - t_B) - t_{B,r}\right], \tag{3.20}$$

$$\begin{aligned} R_{,rr} = {} & \left[\frac{M_{,rr}}{M} - \frac{2M_{,r}\,E_{,r}}{ME} + \frac{2{E_{,r}}^2}{E^2} - \frac{E_{,rr}}{E}\right] R \\ & + \left[\left(\frac{3}{2}\frac{E_{,rr}}{E} - \frac{9{E_{,r}}^2}{4E^2} + \frac{2M_{,r}\,E_{,r}}{ME} - \frac{M_{,rr}}{M}\right)(t - t_B) - \frac{E_{,r}}{E}\ t_{B,r} - t_{B,rr}\right] R_{,t}\,, \\ & - \frac{M}{R^2}\ \left[\left(\frac{3}{2}\frac{E_{,r}}{E} - \frac{M_{,r}}{M}\right)(t - t_B) - t_{B,r}\right]^2. \end{aligned} \tag{3.21}$$

4. The extremum of R along a ray

The following holds at an extremum of $R(t, r)$ along the curve tangent to k^α,

$$\frac{dR}{d\lambda} = R_{,t}\, k^t + R_{,r}\, k^r = 0. \tag{4.1}$$

On future-directed curves $k^t > 0$, so $R_{,t}\, k^t > 0$ when the model expands and $R_{,t}\, k^t < 0$ when it collapses. When shell crossings and necks are absent, $R_{,r} > 0$ [8]. Thus, solutions of (4.1) may exist only where $R_{,t}\, k^r < 0$. On a null geodesic,

(4.1) implies, via (3.12)

$$R,_t{}^2 \left[\frac{(R,_r\, k^r)^2}{1+2E} + \frac{C^2}{R^2} \right] = (R,_r\, k^r)^2 \,. \tag{4.2}$$

Using (2.2) with $\Lambda = 0$ in this we obtain

$$\left(\frac{2M}{R} - 1 \right) (R,_r\, k^r)^2 + \left(\frac{C R,_t}{R} \right)^2 \quad (1+2E) = 0. \tag{4.3}$$

Where $R < 2M$, both terms in (4.3) are nonnegative, so (4.3) may hold only when both are zero. The only physically meaningful situation when this happens is

$$R,_r = 1 + 2E = 0. \tag{4.4}$$

This is a neck [5]. Apart from this locus, $1 + 2E > 0$ must hold in order that the signature is the physical $(+,-,-,-)$. Other solutions of (4.3) do not exist with $R < 2M$ because.

(1) When $C = 0 = k^r$, the geodesic is timelike, while the locus of $C = R,_r = 0 < 1 + 2E$ is a shell crossing which we assumed not to exist.

(2) $R,_t = 0$ holds at maximum expansion (when $E < 0$), but then $R \geq 2M$ [5]. Thus, the solution of (4.3) is $R = 2M$ only on radial geodesics, where $C = 0$. With $C \neq 0$, (4.3) can have solutions only where $R > 2M$ (see examples in Section 5).

Given the value of C and an initial point p_0, Eqs. (3.12)–(3.16) with (3.6)–(3.7) define a single ray, and then each solution of (4.1)[3] defines a point on that ray. When the values of C are changed with p_0 fixed, those points draw a 2-surface S_{p_0}. When p_0 is moved along an observer's world line, the S_{p_0} surfaces form a hypersurface H in spacetime which touches $R = 2M$ along radial rays, but elsewhere lies in $R > 2M$. We will see in Section 6 that for a noncentral observer the hypersurface H and the locus of $k^\mu{}_{;\mu} = 0$ do not coincide, see Sections 5 and 7 for explicit examples.

Now we calculate $d^2R/d\lambda^2$ from (4.1). To eliminate $dk^t/d\lambda$ and $dk^r/d\lambda$ we use (3.14) and (3.16). We also use the derivative of (2.2) with $\Lambda = 0$ by r,

$$R,_t\, R,_{tr} = \frac{M,_r}{R} - \frac{M R,_r}{R^2} + E,_r \,. \tag{4.5}$$

The end result is

$$\frac{d^2R}{d\lambda^2} = -\frac{M,_r\, R,_r\, (k^r)^2}{1+2E} + \frac{C^2}{R^3} \left(1 - \frac{3M}{R} \right). \tag{4.6}$$

For the model to be physical it is necessary that $\rho > 0$ in (2.3), so $M,_r\, R,_r > 0$ and the first term in (4.6) is nonpositive. The second term is negative (positive) where $R < 3M$ ($R > 3M$). Thus, $d^2R/d\lambda^2 < 0$ where $R \leq 3M$, and if a solution of (4.1) exists then it is a maximum. Where $R > 3M$, the sign of $d^2R/d\lambda^2$ depends

[3] On a given ray, (4.1) may have more than one solution or no solutions. See examples further on.

on the balance between the two terms in (4.6), so both minima and maxima of R may exist;[4] see Section 5.

5. Extrema of R along nonradial rays in an exemplary L–T model

To illustrate the conclusions of Section 4 we now consider a recollapsing L–T toy model that has its Big Bang at $t = t_B(M)$ and its Big Crunch at $t = t_C(M)$, where

$$t_B(M) = -bM^2 + t_{B0}, \tag{5.1}$$

$$t_C(M) = aM^3 + t_{B0} + T_0, \tag{5.2}$$

with $a = 10^4$, $b = 200$, $t_{B0} = 5$ and $T_0 = 0.1$ being constants; the mass function M is used as the radial coordinate [4, 5]; see footnote 2 in Section 2. This model is spatially infinite and becomes spatially flat at $M \to \infty$; see Fig. 2. Its subspace $\vartheta = \pi/2$ can be imagined by rotating any panel of Fig. 2 around the $M = 0$ axis.

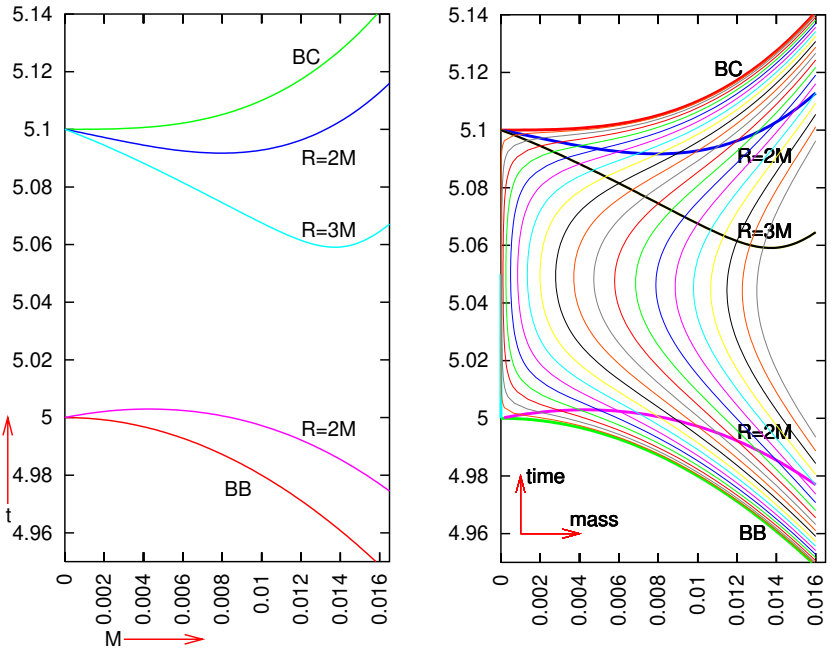

Fig. 2. Left panel: The $t(M)$ profiles of the Big Bang (BB), Big Crunch (BC), both $R = 2M$ sets and of the future $R = 3M$ set in the L–T model given by (5.1)–(5.2). **Right panel:** Contours of constant R written into the left panel. The $R = 0$ contour consists of the BB, the line $M = 0$ and the BC. Values of R increase from left to right at steps of 0.002, from 0 to 0.04 on the rightmost contour.

[4]For radial geodesics $C = 0$, so $d^2R/d\lambda^2 < 0$ and only maxima are possible.

From (2.6) we obtain

$$E(M) = -\frac{1}{2}\left(\frac{2\pi M}{t_C - t_B}\right)^{2/3} = -\frac{1}{2}\left(\frac{2\pi M}{aM^3 + bM^2 + T_0}\right)^{2/3}. \tag{5.3}$$

In this model let us consider the locus of extrema of R along bundles of future-directed rays emitted from the observer world line at $(M, \varphi) = (0.012, 0)$. Figs. 3 and 4 show this locus for rays emitted at 16 points that run in the $\vartheta = \pi/2$ hypersurface.[5] The earliest emission point has $t = 5.075$, the later ones are $\Delta t = 0.0014$ apart, the last one at $t = 5.096$ is close below the $R = 2M$ hypersurface which this observer would cross at $t = 5.0962668$. For each emission point there are 512 rays emitted in initial directions inclined by $\pi/256$ to each other. For more details of this family of rays see Appendix A.

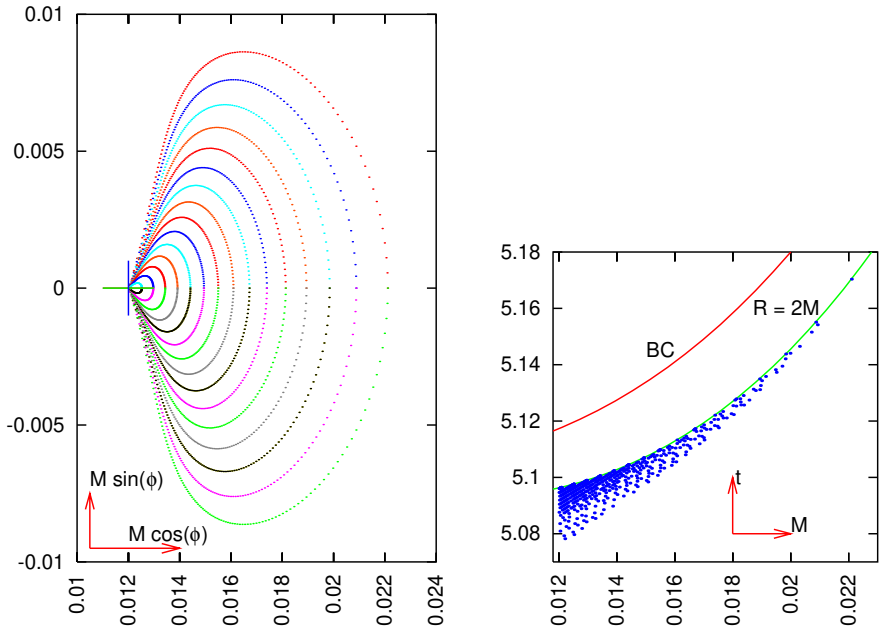

Fig. 3. Left: Loci of R maxima for 16 bundles of rays emitted from the observer world line at $M = 0.012$ in the model of (5.1)–(5.2), projected on a t = constant surface. The rays lie in the $\vartheta = \pi/2$ hypersurface. The cross marks the $(M, \varphi) = (0.012, 0)$ coordinates of the emitter. See the text for details. **Right:** The (M, t) coordinates of all R maxima.

The left panel of Fig. 3 shows the projections of loci of R maxima on a surface of constant $t = t_0$. (In comoving coordinates, the projection does not depend on t_0. This is not an isometric image because a $\{t$ = constant, $\vartheta = \pi/2\}$ surface in an

[5]If the emission point lies early enough, then some or all rays will escape to infinity; on them R need not have extrema. An example is the ray marked "out" in the left panel of Fig. 4.

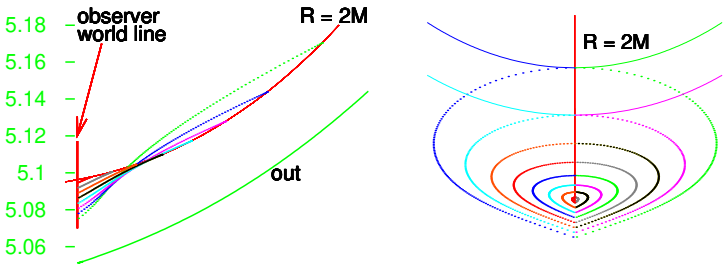

Fig. 4. Left: Projections of selected contours of R maxima on the surface $\varphi = 0$. The line marked "out" is a ray that escapes to $R = \infty$ with no R extrema. **Right:** Projections of the same contours on the surface $\varphi = \pi/2, 3\pi/2$. See the text for more comments.

L–T model is not flat when $E \neq 0$, see (2.1).) There are no R minima for these emission points, and on rays which go off the initial point with $k^r_o \leq 0$ there are no maxima either. The ring of R maxima for the latest emission point coincides with the center of the cross at the scale of the figure. The locus of all R maxima is in this case a curved cone with the vertex at the intersection of the observer world line with the $R = 2M$ hypersurface. As predicted, all maxima occur at $R \geq 2M$ — the right panel of Fig. 3 shows this.

We considered rays running in the $\vartheta = \pi/2$ hypersurface, but in view of comment (3.8) this is not a great limitation. The whole bundle of rays emitted from a fixed initial point consists of sub-bundles, each of which contains rays running in a different $\vartheta' = \pi/2$ hypersurface where ϑ' is related to ϑ by a rotation around a point. So, the complete projection of the whole set of R maxima on a 3-dimensional space of constant t can be imagined by rotating the left panel of Fig. 3 around the $\varphi = 0$ semiaxis.

Fig. 4 shows the projections of odd-numbered rings 1, ..., 15 of R maxima on the $\varphi = 0$ surface (left panel) and on the $\varphi = \pi/2, 3\pi/2$ surface (right panel, horizontal scale smaller than in Fig. 3). The rings are not plane curves. The intersections of the lines in the left panel are artifacts of the projection; the only true points of contact between $R = 2M$ and the maximum R rings are on radial rays. In the right panel, the continuous lines are intersections of the $R = 2M$ surface with the planes of constant $x = M \cos\varphi$.

The locus of R extrema in Figs. 3 and 4 has a simple shape because the emitter world line at $M = 0.012$ is far from the center and the earliest emission point is sufficiently late. The geometry of this locus is more complicated when the comoving emitter is closer to $M = 0$. Consider the extrema of R along bundles of future-directed rays emitted at $(M, \varphi) = (0.005, 0)$, still in the $\vartheta = \pi/2$ hypersurface. Here, as the emission instant progresses toward the future, the contours of R extrema undergo an interesting evolution illustrated in Figs. 5 and 6. They show the projections (along the cosmic dust flow lines) of the loci of R extrema on a t = constant surface, for rays going off 21 initial points. In the main sequence

of 18 emission points their t coordinates change from $t = 5.05$ at steps of 0.0025 to $t = 5.0925$. The last point is just below the $R = 2M$ surface. In addition, there are 3 emission points with $t = 5.053125 + j \times 0.000625$, where $j = 0, 1, 2$; the rays emitted at them allow for a more detailed view of the evolution of the contours.

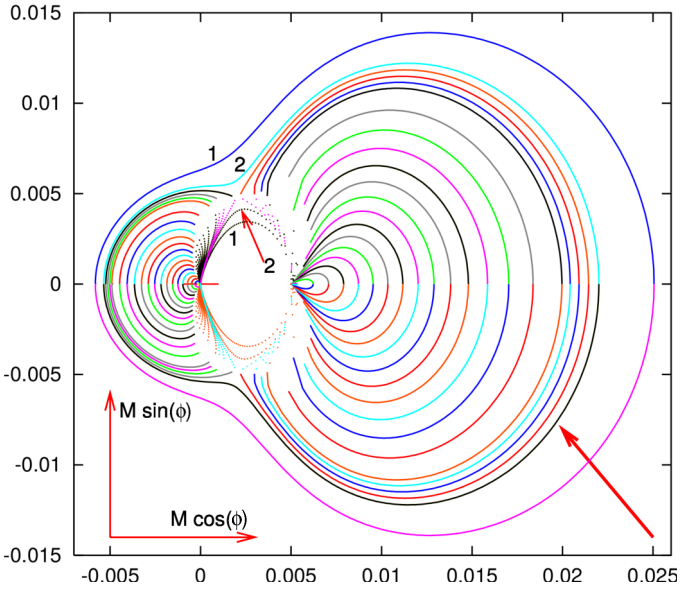

Fig. 5. The loci of R maxima (continuous lines) and minima (dotted lines) along rays going off several emission points on the $(M, \varphi) = (0.005, 0)$ emitter world line, projected on a $\{t = \text{constant}, \vartheta = \pi/2\}$ surface along the dust flow lines. See the text for details, and Fig. 6 for an enlarged view of the region around the tip of the small arrow.

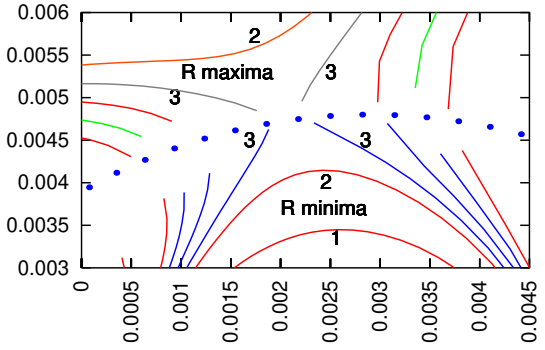

Fig. 6. A closeup view of the region in Fig. 5 where the loops of R extrema change geometry. The arc of large dots separates the loci of maxima from the loci of minima.

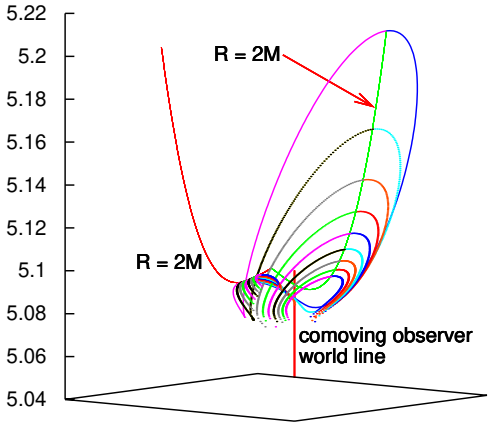

Fig. 7. A 3d view of the loci of R extrema on contours $1, 2, 6, \ldots, 12$.

At each initial point 512 rays were emitted, in regularly spaced initial directions just as before. This time, along some rays R has both minima and maxima. In Fig. 5 the loci of maxima are the continuous lines, the loci of minima are the dots. As the emission instant t progresses, the loops at left shrink toward the center of symmetry of the space at $M = 0$. The loops at right shrink toward the emitter world line. The long arrow marks the view direction in Fig. 7 (40° counterclockwise from the $\varphi = 3\pi/2$ semiaxis).

For the two earliest emission points, R has a maximum along every ray, and a minimum along rays going off at sufficiently large angles to the $\varphi = 0$ line. The contours of minima are initially inside the contours of maxima, but approach each other with progressing emission instant (contours 1 and 2 in Figs. 5 and 6). Near to emission instant 1 of the additional sequence, the contours come into contact (curves 3 in Fig. 6). For later emission times the extrema again form two disjoint loops, but each one is outside the other and contains both maxima and minima. Up to emission instant 9 of the main sequence, the Fortran program found at least two R minima on the right-hand loops. For later emission times, R minima exist only on the left-hand loops. On rays that run between the loops R decreases monotonically to 0 at the BC.

As before, in view of comment (3.8), also here the projection of all R extrema on a t = constant space can be imagined by rotating Fig. 5 around the $\varphi = 0$ semiaxis.

The contours of R extrema are again not plane curves, Fig. 7 shows a 3d view of a few of them; they all lie in the $R \geq 2M$ region. The viewing direction is at 85° to the t axis and at 40° counterclockwise from the $\varphi = 3\pi/2$ half-plane.

In order to further visualise the conclusions of Section 4, Fig. 8 shows the $t(M)$ profiles along selected rays of the bundle that created contour 1 in Fig. 5. Rays beyond # 144 have numbers $160 + j \times 16$ with $j = 0, \ldots, 6$; their labels are omitted.

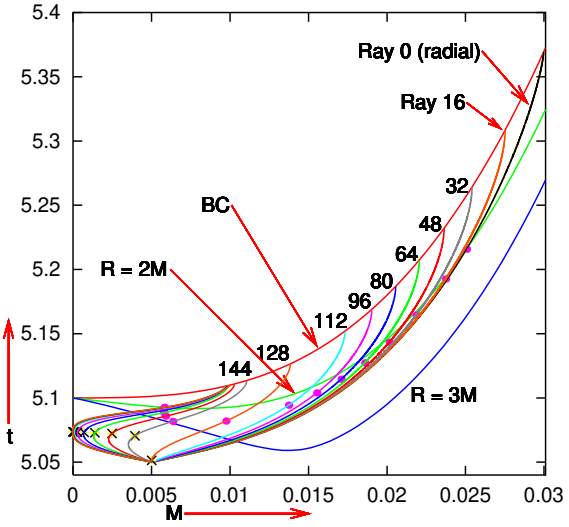

Fig. 8. The graphs of $t(M)$ along selected rays originating at $(M,t) = (0.005, 5.05)$ in the L–T model defined by (5.1)–(5.3). The dots mark the (M,t) coordinates of the maxima of R. On rays 128, ... 256, R has also minima marked by ×s. Note that $2M \le R < 3M$ for all maxima, and $R > 3M$ for all minima.

The dots mark the (M,t) coordinates of the loci of R maxima along the rays; at each one $2M \le R < 3M$. The rightmost and leftmost rays are radial, and along them R is maximum where $R = 2M$. Minima of R exist only along Rays 128 and following, their loci are marked by ×s. At each minimum $R > 3M$.

Fig. 9 shows the projections of selected rays of the earliest-emitted bundle in Fig. 5 on a t = constant surface along the flow lines of the cosmic dust. The large dots and the ×-s mark the $(x,y) \stackrel{\text{def}}{=} (M\cos\varphi, M\sin\varphi)$ coordinates of the points where R is maximum and, respectively, minimum (some extrema are shown without the rays on which they occur). All the extrema lie along contour 1 of Fig. 5. The large circle is at $R = 2M$ on the outward radial Ray 0, where $M = 0.025058$. Each curve ends just before the ray would cross the BC. The vertical stroke marks $M = 0$. The thick arrow marks the view direction in Fig. 10. The meaning of the curve of small dots will be explained in Section 7.

Fig. 9 visualises one more fact: the transition from nonradial to radial rays is discontinuous. Nonradial rays meet the singularity tangentially to r = constant rings while the radial ones meet the singularity orthogonally to those rings.

The right-hand graph in Fig. 10 shows a 3-d image of selected rays from Figs. 8 and 9, and also of the $R = 2M$ hypersurface. It is a map of the $\vartheta = \pi/2$ subspace of the L–T model (5.1)–(5.3) into a Euclidean space with coordinates $(x,y,t) = (M\cos\varphi, M\sin\varphi, t)$. The loop at left is the full ring of maxima of R, i.e. it includes the $x < 0$ half of the bundle (omitted in Fig. 9). The loci of R maxima marked by large dots in the right graph lie along the left half of the loop,

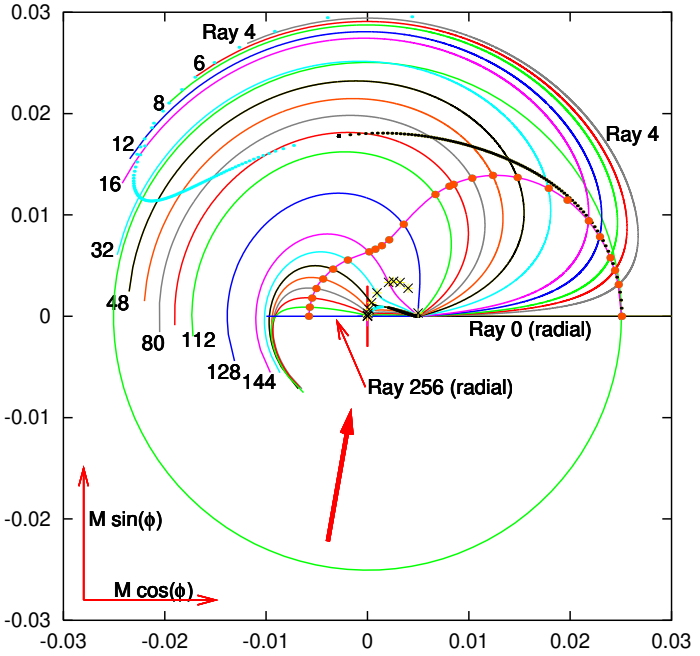

Fig. 9. Projections of selected rays of the earliest bundle in Fig. 5 on a surface of constant t along the flow lines of the cosmic dust. See the text for explanations.

which is further from the viewer. The viewing direction in both graphs, marked by the arrow in Fig. 9, is at 85° to the vertical axis and at 10° clockwise from the $\varphi = 3\pi/2$ half-plane.

6. The set $k^{\mu}{}_{;\mu} = 0$ in a general L–T model

For rays with tangent vectors k^{μ} in the metric (2.1) we have, using (3.6),

$$\theta \stackrel{\text{def}}{=} k^{\mu}{}_{;\mu} \equiv \left(\sqrt{-g}k^{\mu}\right)_{,\mu} / \sqrt{-g}$$

$$= \frac{\sqrt{1+2E}}{R^2 R_{,r} \sin\vartheta}\left[\left(\frac{R^2 R_{,r} \sin\vartheta k^t}{\sqrt{1+2E}}\right)_{,t} + \left(\frac{R^2 R_{,r} \sin\vartheta k^r}{\sqrt{1+2E}}\right)_{,r} + \left(\frac{R^2 R_{,r} \sin\vartheta k^{\vartheta}}{\sqrt{1+2E}}\right)_{,\vartheta}\right]. \quad (6.1)$$

When $C^2 \neq J_0{}^2 > 0$, (6.1) becomes, using (3.7) ($\varepsilon_1 = \pm 1$ is the sign of k^{ϑ}),

$$k^{\mu}{}_{;\mu} = k^t{}_{,t} + k^r{}_{,r} + \left(2\,\frac{R_{,t}}{R} + \frac{R_{,tr}}{R_{,r}}\right)k^t + \left(2\,\frac{R_{,r}}{R} + \frac{R_{,rr}}{R_{,r}} - \frac{E_{,r}}{1+2E}\right)k^r$$

$$+ \frac{\varepsilon_1 C^2 \cos\vartheta}{R^2\sqrt{C^2\sin^2\vartheta - J_0{}^2}}. \quad (6.2)$$

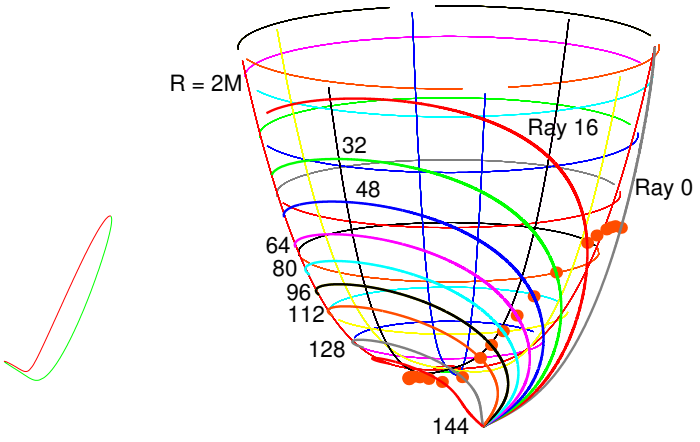

Fig. 10. Right graph: A 3d view of selected rays from Figs. 8 and 9 in the $(M\cos\varphi, M\sin\varphi, t)$ coordinate space. The paraboloid-like surface is the $R = 2M$ locus. **Left graph:** A 3d view of the full ring of maxima of R along rays emitted at $(M, \varphi, t) = (0.005, 0.0, 5.05)$. See the text for details.

When $C^2 = {J_0}^2 > 0$, (3.7) implies $\vartheta = \pi/2$ and $k^\vartheta = 0$. Then the k^ϑ term in (6.1) disappears, and the last term in (6.2) does not arise. This case can be formally included in (6.2) using the convention that the limit of the last term at ${J_0}^2 \to C^2$ is zero.

Using (3.11) and $dk^r/d\lambda = (dk^r/dt)k^t + (dk^r/dr)k^r$, Eq. (3.2) becomes

$$k^t k^r{}_{,t} + k^r k^r{}_{,r} + 2\,\frac{R_{,tr}}{R_{,r}}\,k^t k^r + \left(\frac{R_{,rr}}{R_{,r}} - \frac{E_{,r}}{1+2E}\right)(k^r)^2 - \frac{C^2(1+2E)}{R^3 R_{,r}} = 0. \tag{6.3}$$

Now, we differentiate by t the null condition (3.12),

$$k^t k^t{}_{,t} - \frac{R_{,r}\,R_{,tr}}{1+2E}\,(k^r)^2 - \frac{{R_{,r}}^2}{1+2E}\,k^r k^r{}_{,t} + \frac{C^2 R_{,t}}{R^3} = 0. \tag{6.4}$$

We multiply (6.3) by ${R_{,r}}^2 k^r/(1+2E)$, (6.4) by k^t and add. The result is

$$\frac{(R_{,r}\,k^r)^2}{1+2E}\left[k^r{}_{,r} + \frac{R_{,tr}}{R_{,r}}\,k^t + \left(\frac{R_{,rr}}{R_{,r}} - \frac{E_{,r}}{1+2E}\right)k^r\right] + \frac{C^2}{R^3}\left(R_{,t}\,k^t - R_{,r}\,k^r\right) + \left(k^t\right)^2 k^t{}_{,t} = 0. \tag{6.5}$$

We now calculate $k^t{}_{,t}$ from (6.5) and substitute it in (6.2) obtaining

$$k^\mu{}_{;\mu} = 2\,\frac{R_{,t}}{R}\,k^t + 2\,\frac{R_{,r}}{R}\,k^r + \frac{\varepsilon_1 C^2\cos\vartheta}{R^2\sqrt{C^2\sin^2\vartheta - {J_0}^2}} + \frac{C^2}{(k^t)^2 R^2}\left[-\frac{R_{,t}\,k^t - R_{,r}\,k^r}{R} + k^r{}_{,r} + \frac{R_{,tr}}{R_{,r}}k^t + \left(\frac{R_{,rr}}{R_{,r}} - \frac{E_{,r}}{1+2E}\right)k^r\right]. \tag{6.6}$$

For the solutions of $k^{\mu}{}_{;\mu} = 0$ in the collapse phase of the model there are four cases:

(1) For outward radial rays $C = 0$, so $k^{\mu}{}_{;\mu} = 2\,(R_{,t}\,k^t + R_{,r}\,k^r)\,/R$. Then the loci of $\theta = 0$ and of maximum R coincide and are at $R = 2M$ [5].

(2) For inward radial rays $\theta \neq 0$ all along. This follows from (6.6): on radial rays $C = 0$, so $\theta = 0$ would coincide with $R_{,t}\,k^t + R_{,r}\,k^r = 0$. But on an inward ($k^r < 0$) future-directed ($k^t > 0$) ray in the collapse phase ($R_{,t} < 0$) we have $R_{,t}\,k^t + R_{,r}\,k^r < 0$ all along because $R_{,r} > 0$ (no shell crossings).[6]

(3) On nonradial rays ($C \neq 0$), $R_{,t}\,k^t + R_{,r}\,k^r = 0$ does not fulfil $k^{\mu}{}_{;\mu} = 0$ identically, so the locus of $\theta = 0$ in general does not coincide with the locus of extrema of R (but see footnote 1 in Section 1; see also Figs. 14 and 21 for exceptions). Then

(3a) For rays with $J^2 = C^2$, which stay in $\vartheta = \pi/2$, solutions of $k^{\mu}{}_{;\mu} = 0$ (when they exist) determine a curve in a (t, r) surface, and a surface in a (t, r, φ) space.

(3b) When $C^2 > {J_0}^2$, solutions of $k^{\mu}{}_{;\mu} = 0$ determine a 2-surface in the (t, r, ϑ) space, and the locus of $\theta = 0$ is a 3-dimensional subspace of the L–T spacetime.

In case (3) the derivative $k^r{}_{,r}$ in (6.6) goes across the bundle. To calculate it numerically two rays are needed: a G_1 with a given C_1/R_o, and a nearby G_2 with $C_2/R_o \stackrel{\text{def}}{=} C_1/R_o + D$. It must be calculated at constant t, ϑ and φ, so for each point p_1 on G_1 we find the point p_2 on G_2 with the same (t, ϑ, φ), where $r = r_2$ and $k^r = k^r_2$. Then

$$k^r{}_{,r} \approx \frac{k^r_2 - k^r_1}{r_2 - r_1}. \tag{6.7}$$

All other quantities in (6.6) are intrinsic to a single geodesic. In fact, nothing depends on φ in (6.6), and in case (3a) nothing depends on ϑ either; then it suffices to find a point on G_2 with the same t. For more comments on (6.7) see Appendix B.

At such points where $r_2 = r_1$ but $k^r_2 \neq k^r_1$, $|k^r{}_{,r}| \to \infty$ and may jump between $\pm\infty$. This may be a real effect or a numerical artefact. Note that a real jump of $k^r{}_{,r}$ may only be from $-\infty$ to $+\infty$, and the same is true for θ — see Appendix C for a proof. This has a geometrical interpretation: the jump from $\theta = -\infty$ to $\theta = +\infty$ means that the ray bundle was refocussed to a point and then disperses; the opposite is hard to imagine.

In case (3b), for each initial point and each given C, one has to consider the bundle of rays with the same C and all J_0 allowed by (3.9). A graphical representation of such an object would be a problem in itself, so, for this introductory study, we shall consider the case (3a) only. But, in view of remark (3.8), in this way we disallow only the auxiliary nearby rays with ${J_0}^2 < C^2$ because the (ϑ, φ) coordinates can be adapted to each sub-family of the main rays that proceed in the same equatorial hypersurface.

---

[6] However, it may happen that an inward radial ray flies through the center $M = 0$ and becomes outward on the other side. On the outward segment, point (1) applies. See examples in Sections 5 and 7.

7. The set $k^{\mu}{}_{;\mu} = 0$ in the exemplary L–T model of Section 5

We first consider bundles of rays going off the same observer world line $(M, \varphi) = (0.012, 0)$ as in Figs. 3 and 4 — see Figs. 11 and 12. The origins of the bundles are here at points 1, 4, 7, 10, 13 and 16 of the former set (here labelled 1, ..., 6) and the additional point 7 at $(M, t) = (0.012, 5.1002)$. At point 7 $R > 2M$ (for this observer $R = 2M$ is at $t = 5.09627$). In each bundle there are 512 main rays distributed in the same way as before. Let $C/R_o = d_1$ for the main ray and d_2 for the auxiliary ray used to calculate $k^r{}_{,r}$. The auxiliary rays have $d_2 = d_1 + 1/1024$ for main Rays 1–127 and $d_2 = d_1 - 1/1024$ for main Rays 128–255 (so each auxiliary ray goes off at a larger angle to the $\varphi = 0$ semiaxis than the main ray.) The loci

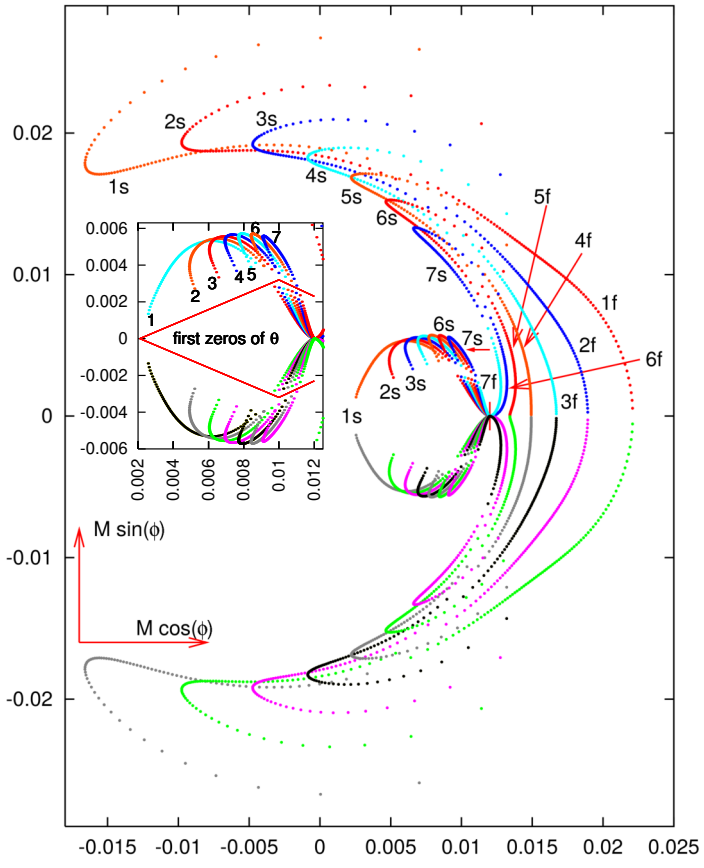

Fig. 11. Main panel: Loci of $\theta = 0$ for rays emitted at 7 selected instants on the world line $(M, \varphi) = (0.012, 0)$ (marked by the vertical stroke) in the model (5.1)–(5.3), projected on a surface of constant t. **Inset:** A closeup view on the central blob. Labels refer to the emission instants. See the text for explanations.

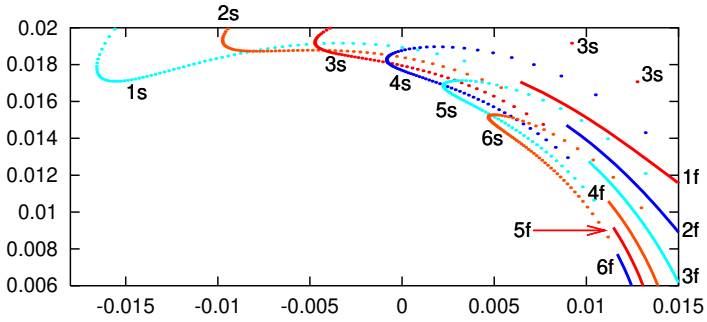

Fig. 12. A closeup view on the upper part of Fig. 11.

of $\theta = 0$ for Rays 257–511 are found by inverting the $y = M \sin\varphi$ coordinates of those on Rays 1–255.

For each emission point, θ has no zeros along several rays. For example, for point 1 at $t = 5.075$, there are no θ zeros on Rays 79–178 (and on their mirror-images 334–433) and on the inward radial ray. On each outward radial ray, θ has a single zero. On most remaining rays θ has two zeros. On each boundary ray between those with two zeros and those with no zeros θ has a single zero. The meaning of the symbols in Figs. 11 and 12 is: 1f = initial point 1, first zero of θ, 1s = initial point 1, second zero of θ, 2f = initial point 2, first zero, etc. The inset in Fig. 11 shows the central blob enlarged; the numbers in it identify the emission points. Rays with no θ zeros run between the blob and the long dotted arcs. Fig. 12 shows where the arcs of first zeros (continuous lines) go over into the arcs of second zeros (dotted lines), each single zero lies at their contact.

Fig. 13 shows the graphs of $\theta(t)$ along selected rays emitted at point 1 and along Ray 40 emitted at point 7 (the dotted line). There is a discontinuity between Ray 0 (on which θ has one zero) and the first nonradial ray, on which θ has two zeros. Then the changes proceed continuously up to Ray 255. Rays with a single $\theta = 0$ are between 78 and 79, and again between 178 and 179. There is one more discontinuity between the last nonradial ray and the inward radial Ray 256, on which $\theta < 0$ all along. The vertical strokes mark the $t = 5.075$ coordinate of point 1. The dotted line shows that the $\theta(t)$ profile is still similar when the emission point is in the $R < 2M$ region. On all rays except the two radial ones, θ becomes very large *positive* on approaching the BC, which means that the ray bundles diverge there. On those nonradial rays where θ has no zeros, the bundle is diverging all the time ($\theta > 0$, but not monotonic, see graphs 85 and 168).

Fig. 14 shows the t coordinates of the loci of maximum R, of both $\theta = 0$ and of $R = 2M$ on all 256 rays emitted at point 1 with $k^\varphi \geq 0$. The ray-number j is related to the angle α_j between the initial direction of the ray and the $\varphi = 0$ semiaxis by $\alpha_j = j\pi/256$. The $\theta = 0$ curves intersect the $R = 2M$ curve at two points, so there exist nonradial rays on which one locus of $\theta = 0$ is at $R = 2M$. The

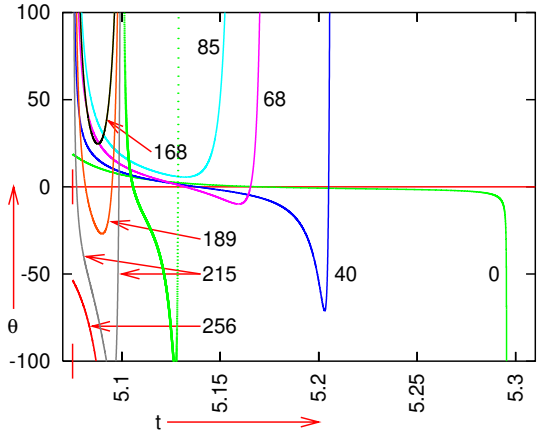

Fig. 13. The graphs of $\theta(t)$ along selected rays emitted at $(M, t) = (0.012, 5.075)$ (the continuous curves) and $(0.012, 5.1002)$ (the dotted curve).

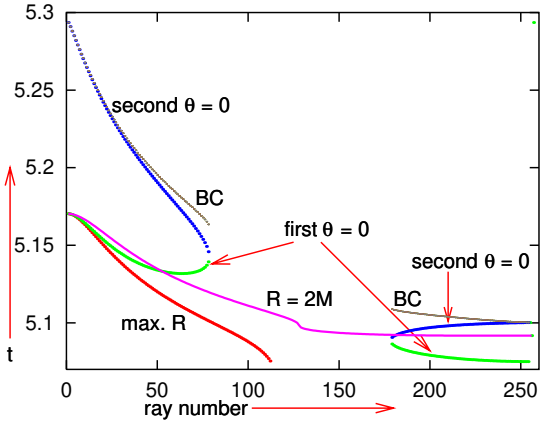

Fig. 14. The t coordinates of various events on rays emitted at $(M, t) = (0.012, 5.075)$.

dotted curve marked “BC" is the graph of t at BC at that M where the second $\theta = 0$ occurred on the ray (*not to be confused* with t at which the ray hits the BC!). It demonstrates that the locus of the second $\theta = 0$ approaches the BC when $\alpha_j \to 0, \pi$, so the loose ends of the dotted curves in Fig. 11 are near the BC. The time-ordering of $\theta = 0$ and $R = 2M$ in Fig. 14 changes from ray to ray. This has physical consequences, to which we will come back in Section 8.

Fig. 15 shows the projections of the $\theta = 0$ curves corresponding to emission points 1, 3 and 5 on the $y = M \sin\varphi = 0$ surface. The upper ends of both branches of the 1s, 3s and 5s arcs are close to the BC. Fig. 16 shows the $y \geq 0$ halves of the same $\theta = 0$ curves as in Fig. 15, this time projected on $x = M \cos\varphi = 0$ surface.

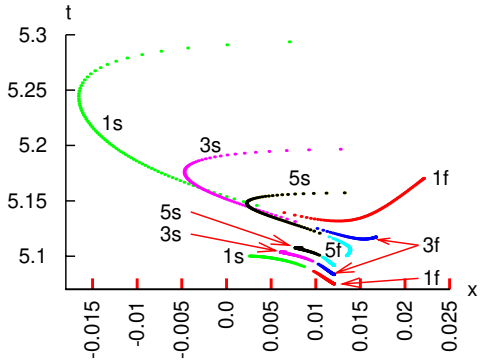

Fig. 15. The $\theta = 0$ curves corresponding to emission points 1, 3 and 5 from Fig. 11 projected on the $y = M \sin\varphi = 0$ surface.

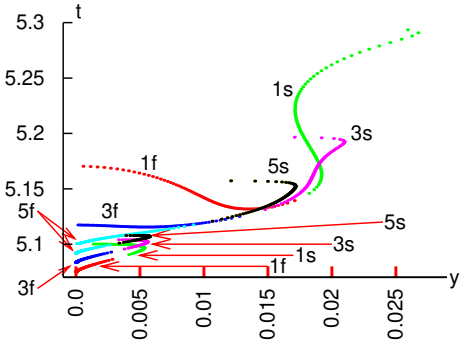

Fig. 16. The $\theta = 0$ curves corresponding to emission points 1, 3 and 5 from Fig. 11 projected on the $x = M \cos\varphi = 0, y \geq 0$ half-plane.

Since the three projections are somewhat entangled, Fig. 17 shows the curves for emission points 3 and 5 separately, at the same scale as in the previous figures.

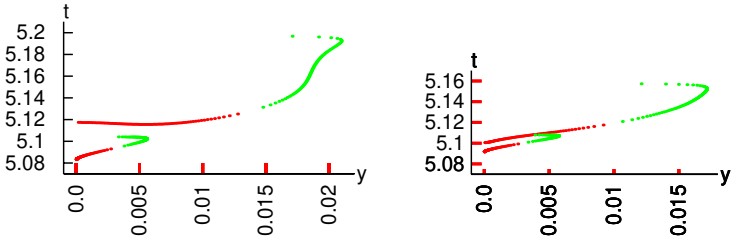

Fig. 17. The $\theta = 0$ curves for emission points 3 (at left) and 5 (at right) from Fig. 16. The first θ zeros are to the left of the gap in each curve, the second zeros are to the right.

Now we consider ray bundles emitted on the world line $(M, \varphi) = (0.005, 0)$. The instants of emission are at $t = 5.05 + k \times 0.0085$, where $k = 0, 1, \ldots, 5$. (The latest and earliest emission points are the same as for the ray bundles used in Fig. 5.) At each of these instants, 512 rays are emitted in regularly spaced initial directions, just as before.

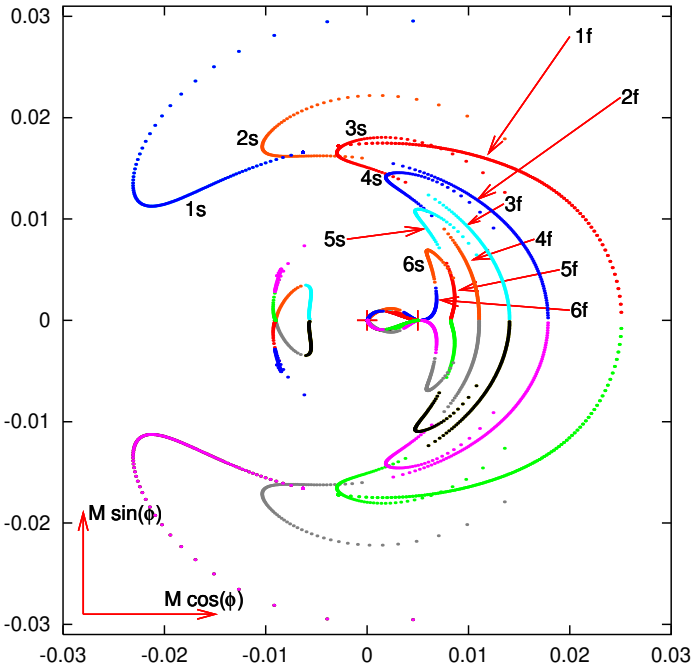

Fig. 18. The analogue of Fig. 11 with the origins of the ray bundles at $(M, \varphi) = (0.005, 0)$. The knot to the left of $M = 0$ is the locus of 3rd, 4th, 5th and 6th θ zeros on the earliest bundle of rays. See Fig. 20 and explanations in the text.

This time, along some rays θ has 3 to 6 zeros. For example, in the bundle emitted at point 1, θ has two zeros on Rays 1–104 and 177–196, no zeros on Rays 105–176, four zeros on Rays 197–206 and six on Rays 207–254. Three zeros exist on a ray between 196 and 197 and 5 on one between 206 and 207. Ray 255 is different: its $\theta(t)$ profile is similar to curve 250 in Fig. 24, except that it begins with $\theta < 0$, so it has 5 zeros. Ray 256 passes through $M = 0$ and becomes outward on the other side, where θ has a single zero at $R = 2M$. The reason of more θ zeros is that the emitter world line is now close to $M = 0$, so some rays fly near the center and later recede from it.

Fig. 18 shows the projections on a surface of constant t of the loci of the first two θ zeros on each ray for all emission points, and the loci of zeros # 3, ..., 6 for emission point 1 (this is the knot left of $M = 0$). The upper half of the largest contour is shown in small dots in Fig. 9. The projection of the emitter world line

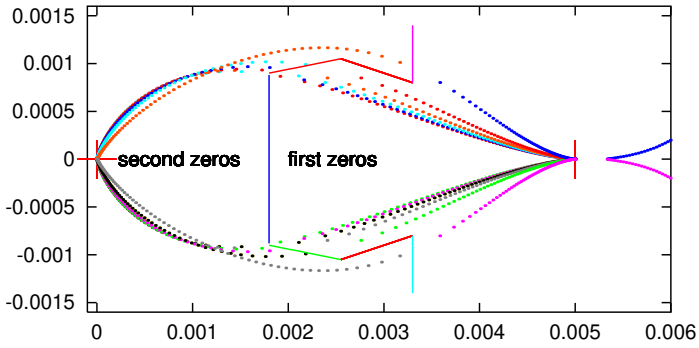

Fig. 19. A closeup view on the central blob in Fig. 18. The loop with the largest vertical diameter corresponds to emission point 6; the vertical diameters decrease when proceeding from point 6 to point 1.

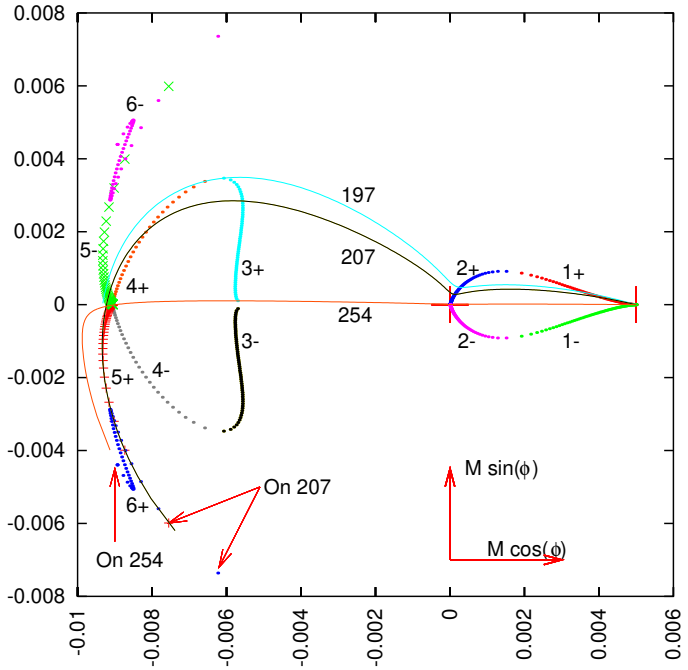

Fig. 20. The knot in Fig. 18 enlarged. See the text for explanations.

is marked with the vertical stroke, the cross marks the center $M = 0$. The meaning of the labels is the same as in Fig. 11. Figure 19 shows a closeup view on the central part of Fig. 18.

Fig. 20 shows the knot in Fig. 18 enlarged. This is the collection of loci of θ zeros # 3, ..., 6 for emission point 1. The numbers label the consecutive zeros; a "+" means that the ray on which the zero lies had $k_o^\varphi > 0$, a "−" means $k_o^\varphi < 0$.

Projections of 3 rays on the plane of the figure are shown in addition, to clarify the ordering of the zeros on the rays. Ray 197 is the first one with four θ zeros,[7] Ray 207 is the first one with 6 zeros, Ray 254 is the last one with 6 zeros. The arcs of 5th zeros (drawn in +-s and ×-s) and 6th zeros partly overlap in this projection. The arrows point to the loci of the 5th and 6th θ zeros on Ray 207 and of the 6th θ zero on Ray 254 (Appendix D explains why the 6th zeros seem to lie beyond the endpoints of the rays.)

Fig. 21 is analogous to Fig. 14. The loci of the 6th θ zeros approach the BC when $\alpha_j \to \pi$. The dotted arc marked BC6 in the left panel of Fig. 22 contains

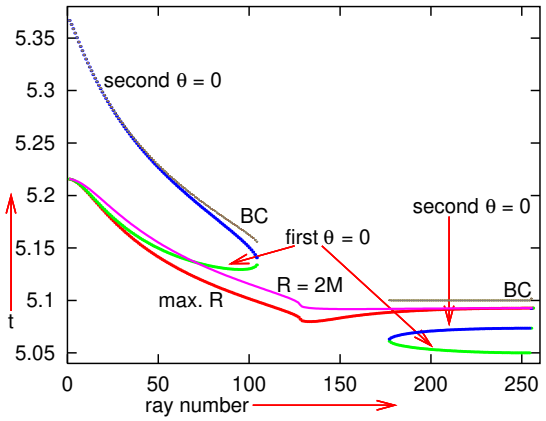

Fig. 21. The analogue of Fig. 14 for the bundle of rays going off the point $(M, t) = (0.005, 5.05)$. See comments in the text.

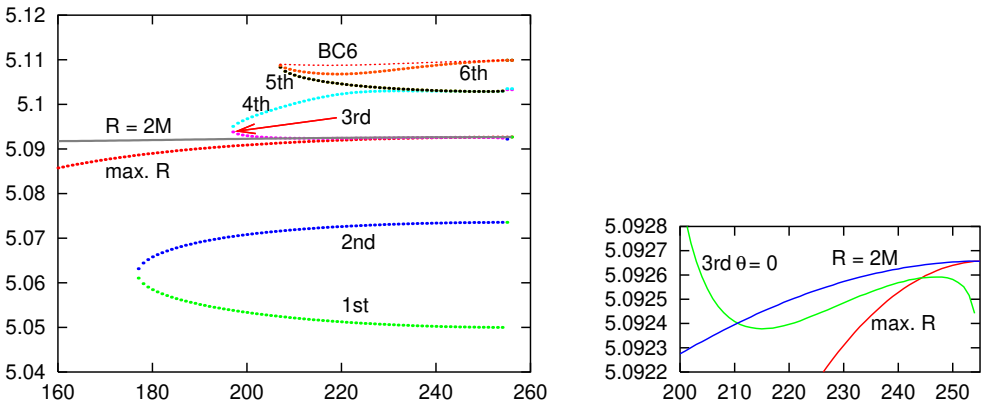

Fig. 22. Left: The lower right corner of Fig. 21 enlarged. See comments in the text. **Right:** Enlarged view on the intersection region between $R = 2M$ and the third $\theta = 0$.

[7]The image of Ray 197 is discontinued at $\varphi \approx \pi$ to avoid clogging the picture.

the t coordinates of the BC at those M where the rays pass the locus of the 6th zero. The loci of second zeros approach the BC when $\alpha_j \to 0$. The arc of third zeros is distinct from $R = 2M$ except at the single intersection point, see the right panel.

Fig. 23 shows profiles of $\theta(t)$ along two rays with 4 θ zeros. On the rays with two θ zeros, the profiles of $\theta(t)$ are similar, except that $\theta > 0$ at the second minimum, like on Ray 190. Somewhere between Rays 197 and 198 there is one on which θ has 3 zeros.

Fig. 24 shows $\theta(t)$ profiles along exemplary rays with six θ zeros. Between Rays 206 and 207 there is one with 5 zeros. On Ray 220, to the right of the 4th zero, θ has a jump from $31,243$ to $-60,253$. This is interpreted as a continuous change, too rapid to be faithfully followed by the Fortran program. The $t \approx 5.1045$ coordinate of this jump is marked with the vertical stroke; it is the locus of the 5th θ zero on this ray.

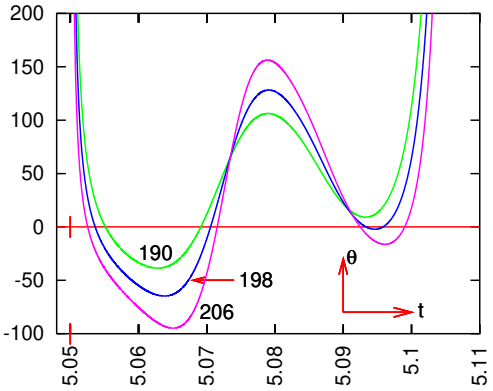

Fig. 23. Profiles of $\theta(t)$ along Rays 198 and 206 on which θ has 4 zeros. Ray 190, where θ has 2 zeros, is shown for comparison. See remarks in the text.

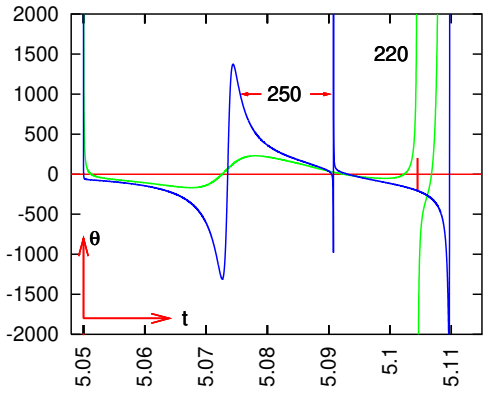

Fig. 24. Typical profiles of $\theta(t)$ on rays with 6 zeros. See remarks in the text.

Figs. 25 and 26 show selected curves from Fig. 18 projected on the $y = M \sin\varphi = 0$ and $x = M \cos\varphi = 0$ coordinate planes, respectively. They are the $\theta = 0$ contours

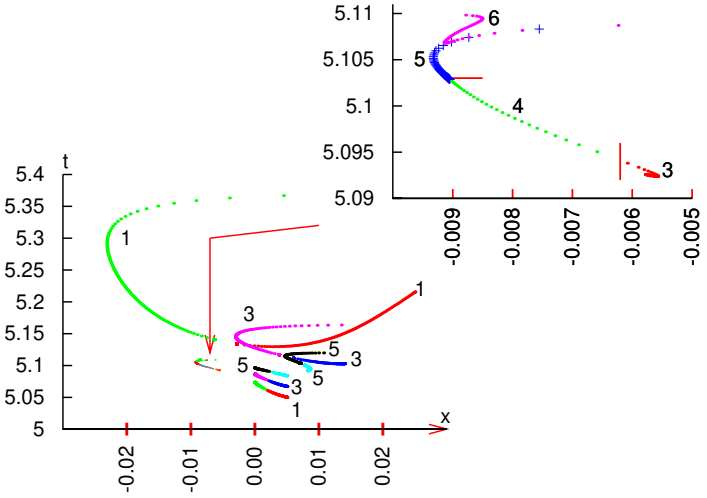

Fig. 25. Main panel: The contours corresponding to emission points 1, 3 and 5 from Fig. 18 projected on the $y = M \sin\varphi = 0$ plane. Labels refer to the emission points. **Inset:** Enlarged view on the loci of zeros # 3, . . . , 6 for the earliest emission point, in the same projection. Here the labels refer to the consecutive number of a θ-zero.

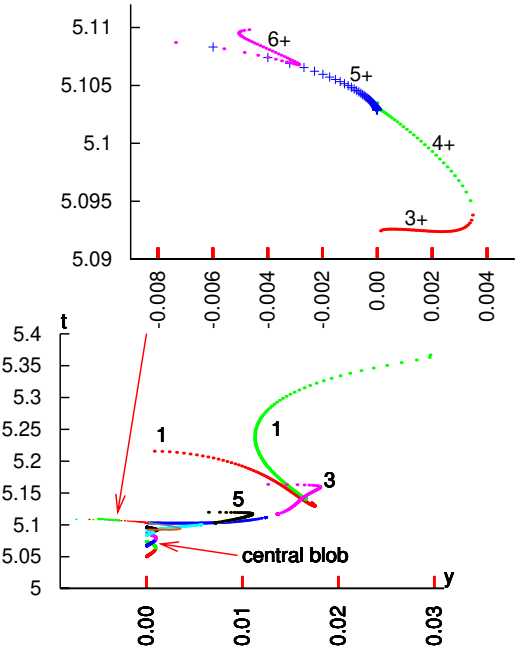

Fig. 26. The $y \geq 0$ halves of the $\theta = 0$ contours from Fig. 25 and the loci of zeros 3, . . . , 6 for emission point 1 projected on the $x = M \cos\varphi = 0$ plane.

corresponding to emission points 1, 3 and 5 (set I) and the contours of zeros # 3, ..., 6 for emission point 1 (set II). The inset in Fig. 25 is a closeup view on set II. The vertical bar is at the border between the loci of the 3rd and 4th zeros. The loci of the 4th and 5th zeros partly overlap, the overlap zone is marked with the horizontal bar. Fig. 26 shows the $y \geq 0$ half of set I and all of set II projected on the $x = M \cos \varphi = 0$ plane.

8. Summary and conclusions

The aim of this paper was to calculate the loci of maximum R and of $\theta \equiv k^{\mu}{}_{;\mu} = 0$ for bundles of rays sent from noncentral events in L–T models (k^{μ} is the tangent vector field to the rays). It turned out that the apparent horizon (AH) of the central observer, located at $R = 2M$, still plays the role of the AH for noncentral observers, at least in the exemplary model introduced in Section 5. The loci of (1) maximum R and of (2) $\theta = 0$ of noncentral observers do not play the role of one-way membranes for light rays, while (3) $R = 2M$ does. This is a summary of the reasoning that led to this conclusion:

Sections 1–3 introduced general preliminaries.

In Section 4, the equation defining a local extremum of the areal radius R along a light ray was derived and discussed for a general L–T model. It was shown that on nonradial rays it can exist only in the $R > 2M$ region. If it occurs in $R < 3M$, then it is a maximum. In $R > 3M$ both minima and maxima are possible (but may not exist).

In Section 5 the results of Section 4 were applied to the exemplary toy model (ETM) introduced in [4, 5]. The loci of R extrema were numerically calculated for rays originating at selected events on two exemplary noncentral cosmic dust world lines in the recollapse phase of the model and running in the equatorial hypersurface $\vartheta = \pi/2$ (EHS). On some nonradial rays R simply decreases to 0 achieved at the BC with no extrema. On some other rays, R has only maxima, on still other ones it has both minima and maxima. The latter can happen when the ray leaves the light source toward decreasing R (which is impossible when the source is at the center where $R = 0$).

In Section 6, the equation of the locus of $\theta = 0$ for a bundle of light rays in a general L–T model was derived. Except on outward radial rays, this locus is different from that of an extremum of R. To calculate θ along a nonradial ray numerically, an auxiliary nearby ray is needed because the derivative $k^{r}{}_{,r}$ in the formula for θ goes across the bundle. On radial rays θ is determined by quantities intrinsic to a single ray.

In Section 7, the results of Section 6 were applied to the discussion of θ along rays running in the EHS of the same ETM that was used in Section 5. The origins of the ray bundles here lie along the same two cosmic dust world lines as those considered in Section 5. For a given initial point, θ has typically no zeros or two zeros along a ray, and becomes $+\infty$ at the Big Crunch (BC). The only rays on which $\theta \to -\infty$ at the BC are the radial ones. The other exceptional rays are those

on the boundaries between the no-zeros and the two-zeros regions: along each of them θ has one zero, but still tends to $+\infty$ at the BC. When the emitter is close to the center, θ has 4 or 6 zeros along rays passing by the center (resp. 3 or 5 on the boundary rays). The locus of the last θ-zero approaches the BC when the initial direction of the ray approaches radial.

The $\theta(t)$ profile on outward radial rays starts positive, monotonically decreases, goes through only one zero, and tends to $-\infty$ at the BC. This signifies focussing to a point at the BC. On inward radial rays, θ starts negative and monotonically decreases to $-\infty$ at the BC. On other rays, θ starts positive and initially decreases, but then becomes increasing (after going through a minimum or more extrema) and tends to $+\infty$ on approaching the BC. This signifies an infinite *divergence* of the rays near the BC.

Temporal orderings of loci (1)–(3) in the EHS of the ETM were determined. The locus of $\theta = 0$ may lie earlier or later than $R = 2M$ and than the maximum of R, depending on the initial direction of the ray. These orderings have a physical meaning. At a point where $\theta = 0$ at $t = t_{\theta=0} < t_{\mathrm{R=2M}}$, an outward radial ray will go some distance toward larger R. Points with $t_{\mathrm{R=2M}} \leq t < t_{\theta=0}$ had been isolated from the outside world before θ became zero. This shows that for noncentral observers the locus of $R = 2M$ rather than that of $\theta = 0$ is a one-way membrane. Since the locus of maximum R has $t_{\mathrm{maxR}} < t_{\mathrm{R=2M}}$ on all nonradial rays, points in the segment $t_{\mathrm{maxR}} < t < t_{\mathrm{R=2M}}$ are not yet isolated from the communication with the outside world.

In Figs. 11 and 18, the intersections of trapped surfaces [9] with the $\vartheta = \pi/2$ hypersurface would lie between the first and second zero of θ. However, $\theta < 0$ only on finite segments of some rays. Thus, if the trapped surface were evolved into the future along these rays, its intersection with $\vartheta = \pi/2$ would become untrapped after a finite time. Along many rays $\theta > 0$ all the way. On those rays where $\theta < 0$ for a while, it becomes positive eventually, going to $+\infty$ on approaching the BC. Moreover, there exist points on some rays where $\theta < 0$ but $R > 2M$, so they are visible from outside — see above and Figs. 14 and 21. All this shows that the formation of a trapped surface is not the ultimate signature of a black-hole-in-the-making in situations relevant to astrophysics.

So, finally, the hypersurface $R = 2M$ does have a universal meaning in a collapsing L–T model: this is the apparent horizon for all observers that signifies the presence of a black hole behind it. (This meaning of $R = 2M$ was identified by Barnes [10] and Szekeres [11] by considering spherical trapped surfaces surrounding the center of symmetry and the origin, respectively.) Events in the region $R < 2M$ are cut off from communication with the $R > 2M$ part of the spacetime. See [4] for an example of how an L–T model (actually, of the same family as in Section 5) can be applied to the description of a formation of a black hole inside a spherical condensation of dust. This conclusion shows that the transition from an L–T model to the Friedmann (F) limit is discontinuous in one more way: the individual AHs of noncentral observers appear abruptly. (The other discontinuity is the abrupt disappearance of blueshifts in the F limit, first pointed out by Szekeres in another paper [12].)

A. Details of Fig. 3

Rays 0 and 256 are radial (outward and inward, respectively); on them $C = 0$. Rays 1 to 127 have $C > 0$ and $k^r_o > 0$ at the initial points, Ray 128 has $C > 0$ and $k^r_o = 0$, Rays 129 to 255 have $C > 0$ and $k^r_o < 0$. Rays 257 to 511 are mirror images of 1–255.

The exact values of k^r_o are determined by C/R_o via (3.12). The maximum $|C|/R_o = 1$ is on Rays 128 and 384. On Rays 0–128, $C/R_o = j/128$ where $j = 0, 1, \ldots, 128$. On Rays 128–512, $C/R_o = i/128$ where $i = 128, 127, \ldots, 1, 0$. The loci of maxima of R on Rays 257–511 need not be calculated separately, they are found by inverting the signs of $y = M \sin\varphi$ of the loci found for Rays 1–255.

B. Numerical calculation of $k^r{}_{,r}$ in (6.7)

At the initial point, both geodesics referred to in (6.7) begin with $r_2 = r_1$, but $k^r_2 \neq k^r_1$. Consequently, the initial $k^\mu{}_{;\mu} = \infty$, so the calculation is started at step 2.

The following method was used to find p_2 on G_2 with the same $t = t_1$ as p_1 on G_1:

First, the path of the auxiliary nearby ray G_2 is calculated, thereby the collection of values of t_n, r_n and k^r_n, $n = 1, \ldots, N$, along G_2 is found.

Given t at p_1 on G_1 we find the largest $t_n \leq t$ on G_2, and the corresponding r_n and k^r_n on G_2. Then we extrapolate to t by

$$r_2 = r_n + \frac{r_{n+1} - r_n}{t_{n+1} - t_n}\,(t - t_n)\,, \tag{B.1}$$

and similarly for k^r. The r_2 and k^r_2 are then used in (6.7).

C. The sign of an infinite jump of $k^r{}_{,r}$ and θ

This is the proof that an infinite jump of $k^r{}_{,r}$ and θ on a light ray can only be from $-\infty$ to $+\infty$. We assume that $-\infty < k^r < +\infty$ all along the ray. In (6.6) $k^r{}_{,r}$ is multiplied by a nonnegative coefficient, so the sign of an infinite jump in θ must be the same as that in $k^r{}_{,r}$.

Suppose that $k^r{}_{,r} > 0$ at a point where $r_2 \approx r_1$. Then either $r_2 > r_1$ and $k^r_2 > k^r_1$ or $r_2 < r_1$ and $k^r_2 < k^r_1$. In the first case, r_2 increases faster along the ray than r_1, so, as long as both inequalities hold, $r_2 - r_1 \neq 0$. In the second case r_2 decreases faster than r_1, with the same conclusion. In both cases $|k^r{}_{,r}| < \infty$.

Now suppose that $k^r{}_{,r} < 0$ at $r_2 \approx r_1$. Then either $r_2 > r_1$ and $k^r_2 < k^r_1$ or $r_2 < r_1$ and $k^r_2 > k^r_1$. In the first case, r_1 increases faster along the ray than r_2, so may catch up with r_2. In the second case the roles of r_1 and r_2 are reversed and the same conclusion follows. In both cases $k^r{}_{,r}$ will jump from $-\infty$ to $+\infty$. □

D. A comment on Fig. 20

In Fig. 20, on Rays 207 and 254 the last dot marking the 6th zero of θ lies beyond the end of the ray projection. Here is the reason of the spurious paradox:

for the ray paths, one in 100 calculated data points is shown in the figure. This is because the program drawing the graphs could not handle the large numbers of data points that were actually calculated (several $\times 10^5$ in some cases). So, these last points indeed do lie on the calculated ray paths, only the paths were not interpolated to them in the figure.

Acknowledgements

The idea of this paper was born in a discussion (by email) with José Senovilla, in connection with [13]. For some calculations, the computer algebra system Ortocartan [14, 15] was used.

REFERENCES

[1] S. W. Hawking and G. F. R. Ellis: *The Large-scale Structure of Spaceetime*, Cambridge University Press, Cambridge 1973.
[2] G. Lemaître: L'Univers en expansion [The expanding Universe], *Ann. Soc. Sci. Bruxelles* **A53**, 51 (1933); English translation: *Gen. Relativ. Gravit.* **29**, 641 (1997); with an editorial note by A. Krasiński: *Gen. Relativ. Gravit.* **29**, 637 (1997).
[3] R. C. Tolman: Effect of inhomogeneity on cosmological models, *Proc. Nat. Acad. Sci. USA* **20**, 169 (1934); reprinted: *Gen. Relativ. Gravit.* **29**, 935 (1997); with an editorial note by A. Krasiński, in: *Gen. Relativ. Gravit.* **29**, 931 (1997).
[4] A. Krasiński and C. Hellaby: Formation of a galaxy with a central black hole in the Lemaitre–Tolman model, *Phys. Rev. D* **69**, 043502 (2004).
[5] J. Plebański and A. Krasiński: *An Introduction to General Relativity and Cosmology*. Cambridge University Press 2006, 534 pp.
[6] A. A. Friedmann: Über die Krümmung des Raumes [On the curvature of space], *Z. Physik* **10**, 377 (1922); Über die Möglichkeit einer Welt mit konstanter negativer Krümmung des Raumes [On the possibility of a world with constant negative curvature of space], *Z. Physik* **21**, 326 (1924). English translation of both papers *Gen. Relativ. Gravit.* **31**, 1991 and 2001 (1999), with an editorial note by A. Krasiński and G. F. R. Ellis, *Gen. Relativ. Gravit.* **31**, 1985 (1999); addendum: *Gen. Relativ. Gravit.* **32**, 1937 (2000).
[7] V. Perlick: Gravitational lensing from a spacetime perspective, *Living Rev Relativ.* **7** (1): 9 (2004).
[8] C. Hellaby and K. Lake: Shell crossings and the Tolman model, *Astrophys. J.* **290**, 381 (1985) [+ erratum: *Astrophys. J.* **300**, 461 (1985)].
[9] J. M. M. Senovilla: Trapped surfaces, *Int. J. Mod. Phys. D* **20**, 2139 (2011).
[10] A. Barnes: On gravitational collapse against a cosmological background, *J. Phys. A* **3**, 653 (1970).
[11] P. Szekeres: Quasispherical gravitational collapse, *Phys. Rev. D* **12**, 2941 (1975).
[12] P. Szekeres: Naked singularities, in: *Gravitational Radiation, Collapsed Objects and Exact Solutions*, ed. by C. Edwards, Springer (Lecture Notes in Physics, vol. 124), New York, pp. 477–487 (1980).
[13] I. Bengtsson, E. Jakobsson and J. M. M. Senovilla: Trapped surfaces in Oppenheimer–Snyder black holes, *Phys. Rev. D* **88**, 064012 (2013).
[14] A. Krasiński: The newest release of the Ortocartan set of programs for algebraic calculations in relativity, *Gen. Relativ. Gravit.* **33**, 145 (2001).
[15] A. Krasiński and M. Perkowski: *The system ORTOCARTAN – user's manual*, Fifth edition, Warsaw 2000.